Enhancement of laser pulse induced photocurrents by topological states in graphene nanoribbons

Rulin Wang,[1,*] Fuzhen Bi,[2,3] Wencai Lu,[4] Xiao Zheng,[5] and ChiYung Yam[6]

[1]*Centre for Theoretical and Computational Physics, College of Physics, Qingdao University, Qingdao 266071, China*

[2]*Qingdao Institute of Bioenergy and Bioprocess Technology, Chinese Academy of Sciences, Qingdao 266101, China*

[3]*Laboratory of Solar Energy, Shandong Energy Institute, Qingdao 266101, China*

[4]*College of Physics, Qingdao University, Qingdao 266071, China*

[5]*Department of Chemistry, Fudan University, Shanghai 200433, China*

[6]*Shenzhen Institute for Advanced Study, University of Electronic Science and Technology of China, Shenzhen 518000, China*

(Received 6 November 2023; revised 9 May 2024; accepted 10 May 2024; published 22 May 2024)

Electron dynamics driven by few-cycle laser pulses has recently attracted great interest as a means to realizing the manipulation of electron motion on the atomic timescale. Using tight-binding models and the time-dependent nonequilibrium Green's function (TD-NEGF) method, we investigated laser-pulse-induced electron dynamics in armchair graphene nanoribbons (GNRs) with and without topological states. The results show that multiphoton excitations can lead to photocurrents along the GNRs and that the corresponding transferred charges can be enhanced by a factor of several hundreds for GNRs with topological states. This enhancement effect is due to the topological states in the band gap of GNRs, which reduce the order of multiphoton absorption and increase the transition probability of excitations.

DOI: 10.1103/PhysRevB.109.195303

I. INTRODUCTION

Advancements in few-cycle laser-pulse generation offer unique opportunities to study ultrafast electron dynamics in its natural femtosecond timescale [1,2]. The control of electron motion by laser pulses has been explored both experimentally and theoretically. The manipulation of electron motion can be realized by various implementation schemes, such as the laser-controlled charge migration in ionized molecules [3,4], symmetry breaking or symmetry restoration of electronic structure in molecules [5], control of electron motion using synthesized light waveforms in dielectrics [6], and localized surface plasmon resonances in metals [7]. In these schemes, the control of electron motion usually focuses on the ultrafast dynamic process inside the materials. In contrast, for photoelectric devices, the electron moving through the devices is more important, which is the photocurrent driven by a laser pulse. Recently, laser-pulse-induced photocurrents were investigated in the tunneling barrier [8–12] and dielectric [13–15] and semiconductor systems [16–18], and these photocurrents can be modulated by the carrier-envelope phase and central frequency of the laser pulses. In semiconductor devices, laser-pulse-induced photocurrents were found to be determined by the multiphoton excitations and to depend on the band gap of the semiconductor [18]. Thus, the adjustment of the band gap should be a practical, feasible way to control laser-pulse-induced photocurrents through semiconductor devices. In this study, we investigate the effect of in-gap localized states on laser-pulse-induced photocurrents and propose an applicable approach to enhancing photocurrents in semiconductor devices.

Graphene nanoribbons (GNRs) are an ideal platform for investigating laser-pulse-induced photocurrents in semiconductors. Armchair GNRs exhibit a tunable band gap, depending on the width of nanoribbons [19–21]. In bilayer armchair GNRs, the band gap can be continuously adjusted with the control of a vertical electric field [22]. The band engineering of a GNR by edge modification is another route used to control the band gap [23,24], which was implemented experimentally using the on-surface synthesis approach [25–27]. This atomic precision fabrication technique broadens the scope of topological band engineering to quasi-one-dimensional materials. The periodic arrangement of topological states along the GNR backbone enables the control of the band gap, which can be tuned by adjusting the periodic coupling of topological states [28,29]. The coupling includes the intracell coupling t_n between two states in the same dimer and the intercell coupling t_m between two states in neighboring dimers. For edge-extended GNR systems including several topological states, the topological states are usually in the band gap of the GNR backbone, and the energy of in-gap topological states can be controlled by changing the values of t_n and t_m [30]. The effect of these in-gap topological states on real-time electron dynamics, however, has yet to be demonstrated.

Here, we simulate laser-pulse-induced photocurrents in a seven-carbon-atom wide armchair GNR (7-AGNR) with in-gap localized topological states. We consider the situation where the topological states and the area around them were under the irradiation of few-cycle laser pulses. This part of the system is excited into a nonequilibrium state, which is taken as an open system. In contrast, the part away from

*rulin11@qdu.edu.cn

the irradiation region is assumed to be in a thermodynamic equilibrium state, which is taken as the surrounding environment of an open system and provides dissipative channels for the nonequilibrium state [31–33]. The accurate description of the dissipative process is crucial in the calculation of laser-pulse-induced photocurrents. In the framework of the time-dependent nonequilibrium Green's function (TD-NEGF) method, the dissipation term is represented by the energy-dependent spectral function $\mathbf{\Lambda}(\epsilon)$. The value of spectral function $\mathbf{\Lambda}(\epsilon)$ varying with the energy ϵ is related to the coupling between the open system and environment. The large value of $\mathbf{\Lambda}(\epsilon)$ at a specific energy point ϵ indicates the strong coupling between the open system and environment, which would lead to a small relaxation time for the nonequilibrium state of the open system. The small value of $\mathbf{\Lambda}(\epsilon)$ indicates the weak coupling at the corresponding energy point ϵ, which would lead to a large relaxation time for the nonequilibrium state. Thus the different values of $\mathbf{\Lambda}(\epsilon)$ varying with the energy points ϵ indicate the different relaxation times of electron dynamics, so electron dynamics for each energy point should be formulated by a separate equation of motion [34–37]. Moreover, the large number of equations of motion would increase computational costs, making them difficult to implement in practical calculations. One way to reduce the computational costs is the wide-band-limit (WBL) approach [38,39], in which the energy dependence of $\mathbf{\Lambda}(\epsilon)$ is ignored and the value of the spectral function at the Fermi energy is used to replace the energy-dependent spectral function $\mathbf{\Lambda}(\epsilon)$. Thus, the WBL approach is suitable for the simulation of electron dynamics near the Fermi energy. For the simulation of electron dynamics in the system with a band gap, such as 7-AGNR in this work, the electron dynamics away from Fermi energy would play a dominant role in the simulation. Thus, in this work, we adopt a Lorentzian decomposition scheme [40,41] in which the spectral function $\mathbf{\Lambda}(\epsilon)$ is fitted by a set of Lorentzian functions, and each Lorentzian function is related to an equation of motion for electron dynamics. Under the premise of ensuring calculation accuracy, we reduce the number of functions to improve the computational efficiency of the simulation.

II. SIMULATION DETAILS

We simulate the ultrafast electron dynamics driven by the laser pulses in the system of edge-extended 7-AGNR with a single dimer. Figures 1(a) and 1(b) present the structure models for the systems with the dimer $n = 1$ and $n = 3$, respectively. These structures of edge-extended 7-AGNRs are experimentally realized by using an on-surface synthesis approach [29]. In our calculation, the whole system was divided into two parts: an open system [the blue shaded part in Figs. 1(a) and 1(b)] and a surrounding environment (the other part of the system). The environment includes two semi-infinite GNRs on the left and right of the open system. The open system was assumed under irradiation of a laser pulse. The laser pulse was considered linearly polarized light, and the direction of the electric field was parallel to the GNR direction. The time-varying electric field of the laser pulse would lead to a nonequilibrium state inside the open system. The surrounding environment, which was out of range of laser irradiation, was assumed to be in a thermal equilibrium and provided dissipative channels for the nonequilibrium state in the open system.

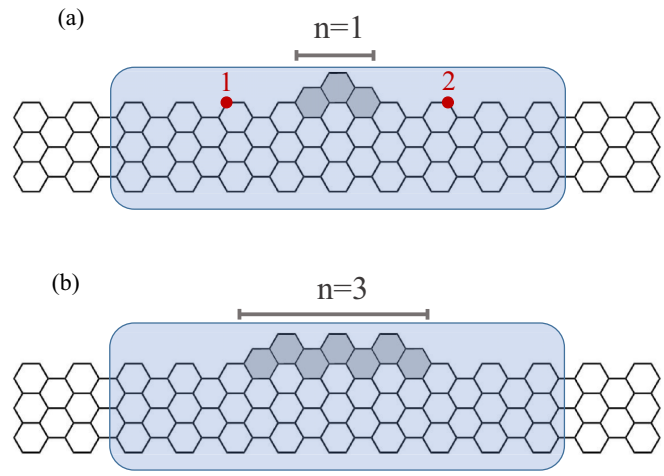

FIG. 1. Schematic diagram of edge-extended 7-AGNR with the dimer (a) $n = 1$ and (b) $n = 3$. The atoms under irradiation constitute the open system (the blue shaded part), while the other part of the system is the surrounding environment of the open system.

A. TD-NEGF method for an open system

The electron dynamics of the open system can be described by the TD-NEGF method, of which the detailed derivations can be found in Refs. [31], [40], and [41]. For the sake of completeness and ease of presentation, we introduce the TD-NEGF method here. The basic equation is an equation of motion (EOM) for the electron dynamics of the open system [31]

$$i\dot{\boldsymbol{\sigma}}_D(t) = [\boldsymbol{h}_D(t), \boldsymbol{\sigma}_D(t)] - i\sum_{\alpha} \boldsymbol{D}_{\alpha}(t), \tag{1}$$

where $\boldsymbol{\sigma}_D(t)$ and $\boldsymbol{h}_D(t)$ are the reduced single-electron density matrix and the Hamiltonian matrix for the device (the open system), respectively. $\alpha = L/R$ denotes the left electrode or right electrode (the environment). $\boldsymbol{D}_{\alpha}(t)$ is the dissipation term for electron dynamics of the device.

We chose the nearest-neighbor tight-binding Hamiltonian to describe the electronic structure of the whole system, including the device and electrodes. The Hamiltonian is given by $\boldsymbol{H} = \sum_i \epsilon_i a_i^{\dagger} a_i + \sum_{ij} \gamma_{ij} a_i^{\dagger} a_j$, where a_i is the annihilation operator for an electron on the site of the ith atom. ϵ_i is the on-site energy and is set to zero for the equilibrium state. In contrast, for the nonequilibrium state induced by a laser pulse, the energy ϵ_i would vary with the electric field of pulse and could be determined by the position of the ith atom. γ_{ij} is the coupling strength between ith atom and its nearest-neighbor jth atom, and the coupling at the GNRs edge has to be increased by 12% owing to the hydrogen passivation of the edge carbon atoms [42]. Thus, the coupling strength for interior carbon atoms is set to the same value of graphene system $\gamma_0 = -2.7$ eV [43], and the coupling strength for edge carbon atoms was set to $\gamma_e = 1.12\ \gamma_0$.

Note that in Eq. (1), $\boldsymbol{h}_D$ represents the Hamiltonian for the device decoupled from electrodes. Moreover, the effect of electrode α on the electron dynamics of the device is described by the term $\boldsymbol{D}_\alpha(t)$, which represents the dissipative process at the boundary of the device and the electrode, such as the exchanges of electrons, energy, and phase information between the device and the electrode.

The accurate description of the dissipation term $\boldsymbol{D}_\alpha(t)$ is essential for the simulation of electron dynamics. In the TD-NEGF method, $\boldsymbol{D}_\alpha(t)$ is expanded with the Green's functions $\boldsymbol{G}^{<,>}(t,t')$ and the self-energies $\boldsymbol{\Sigma}_\alpha^{<,>}(t',t)$, as follows [31,38]:

$$\boldsymbol{D}_\alpha(t) = \int_{-\infty}^{t} dt' [\boldsymbol{G}^{<}(t,t')\boldsymbol{\Sigma}_\alpha^{>}(t',t) - \boldsymbol{G}^{>}(t,t')\boldsymbol{\Sigma}_\alpha^{<}(t',t)] + \text{H.c.}, \tag{2}$$

where $\boldsymbol{G}^{<}(t,t')$ and $\boldsymbol{G}^{>}(t,t')$ are the lesser and greater Green's functions of the open system, respectively. $\boldsymbol{\Sigma}_\alpha^{>}(t',t)$ and $\boldsymbol{\Sigma}_\alpha^{<}(t',t)$ are the greater self-energies and lesser self-energies, respectively, which correspond to the coupling of the device with the electrode α.

With the time-varying electric potential $\Delta_\alpha(t)$ caused by the laser pulse, the self-energies are given by

$$\boldsymbol{\Sigma}_\alpha^{<}(t',t) = \frac{i}{\pi} e^{-i\int_t^{t'} d\tau \Delta_\alpha(\tau)} \int d\epsilon \boldsymbol{\Lambda}_\alpha(\epsilon) f_\alpha(\epsilon) e^{-i\epsilon(t'-t)}, \tag{3}$$

$$\boldsymbol{\Sigma}_\alpha^{>}(t',t) = -\frac{i}{\pi} e^{-i\int_t^{t'} d\tau \Delta_\alpha(\tau)} \int d\epsilon \boldsymbol{\Lambda}_\alpha(\epsilon) [1 - f_\alpha(\epsilon)] e^{-i\epsilon(t'-t)}, \tag{4}$$

where $f_\alpha(\epsilon)$ is the Fermi-Dirac distribution for electrode α and $\boldsymbol{\Lambda}_\alpha(\epsilon)$ is spectral function, which is given by the imaginary part of the retarded self-energy, $\boldsymbol{\Lambda}_\alpha(\epsilon) = -\text{Im}[\boldsymbol{\Sigma}_\alpha^r(\epsilon)]$. In our simulation, the eletrodes consisted of two semi-infinite GNRs, and the spectral function $\boldsymbol{\Lambda}_\alpha(\epsilon)$ could be evaluated using a highly convergent renormalization method [44,45].

Using the dissipation term $\boldsymbol{D}_\alpha(t)$ in Eq. (2) and the self-energies in Eqs.(3) and (4), the EOM Eq. (1) for the density matrix $\boldsymbol{\sigma}_D(t)$ was written by EOMs for a set of variables $\{\boldsymbol{\sigma}_D(t), \boldsymbol{\varphi}_\alpha(\epsilon,t), \boldsymbol{\phi}_{\alpha\alpha'}(\epsilon,\epsilon',t)\}$ [33,34]:

$$i\dot{\boldsymbol{\sigma}}_D(t) = [\boldsymbol{h}_D(t), \boldsymbol{\sigma}_D(t)] - \sum_\alpha \int d\epsilon [\boldsymbol{\varphi}_\alpha(\epsilon,t) - \boldsymbol{\varphi}_\alpha^\dagger(\epsilon,t)], \tag{5}$$

$$i\dot{\boldsymbol{\varphi}}_\alpha(\epsilon,t) = [\boldsymbol{h}_D(t) - \epsilon - \Delta_\alpha(t)]\boldsymbol{\varphi}_\alpha(\epsilon,t) - \frac{1}{\pi}[f_\alpha(\epsilon) - \boldsymbol{\sigma}_D(t)]\boldsymbol{\Lambda}_\alpha(\epsilon) + \sum_{\alpha'} \int d\epsilon' \boldsymbol{\phi}_{\alpha\alpha'}(\epsilon,\epsilon',t), \tag{6}$$

$$i\dot{\boldsymbol{\phi}}_{\alpha\alpha'}(\epsilon,\epsilon',t) = -\frac{1}{\pi}[\boldsymbol{\Lambda}_{\alpha'}(\epsilon')\boldsymbol{\varphi}_\alpha(\epsilon,t) - \boldsymbol{\varphi}_{\alpha'}^\dagger(\epsilon',t)\boldsymbol{\Lambda}_\alpha(\epsilon)] + \left[\epsilon' + \Delta_{\alpha'}(t) - \epsilon - \Delta_\alpha(t)\right]\boldsymbol{\phi}_{\alpha\alpha'}(\epsilon,\epsilon',t), \tag{7}$$

where $\boldsymbol{\varphi}_\alpha(\epsilon,t)$ and $\boldsymbol{\phi}_{\alpha\alpha'}(\epsilon,\epsilon',t)$ are the auxiliary density matrices and the EOMs for these auxiliary density matrices aim to obtain the dissipation term $\boldsymbol{D}_\alpha(t)$. In contrast, the EOMs for the auxiliary density matrices have to be formulated for each energy points ϵ, which would lead to huge computational costs, making it practically impossible to implement in the simulation.

To reduce the computational costs, we deconstruct the spectral function $\boldsymbol{\Lambda}_\alpha(\epsilon)$ and Fermi-Dirac distribution $f_\alpha(\epsilon)$ by Lorentzian functions and the Padé expansion as

$$\boldsymbol{\Lambda}_\alpha(\epsilon) \approx \sum_{l=1}^{N_l} \frac{1}{(\epsilon - \Omega_l)^2 + W_l^2} \bar{\boldsymbol{\Lambda}}_{\alpha l}, \tag{8}$$

$$f_\alpha(\epsilon) = \frac{1}{e^{\beta(\epsilon-\mu_\alpha)}+1} \approx \frac{1}{2} + \sum_{p=1}^{N_p} R_p \left[\frac{1}{\beta(\epsilon-\mu_\alpha) - z_p^+} + \frac{1}{\beta(\epsilon-\mu_\alpha) - z_p^-}\right], \tag{9}$$

where Ω_l and W_l are the centers and widths of the Lorentzian function, respectively; $\bar{\boldsymbol{\Lambda}}_{\alpha l}$ refers to the coefficients determined by a least-square fit; N_l is the number of Lorentzian functions. μ_α is the chemical potential of electrode α; $\beta = [k_b T]^{-1}$ reflects Boltzmann's constant k_b and the system temperature T; R_p and $z_p^\pm$ are the coefficients and singular points determined by the Padé expansion [46], respectively; N_p is the number of Padé terms.

By inserting Eqs. (8) and (9) into Eqs. (3) and (4), and using the residue theorem, we would turn the integral of energy ϵ in Eqs. (3) and (4) into a summation for the poles of Lorentzian and Padé functions. In this way, the variables of EOMs in Eqs. (5) to (7) would be replaced by $\{\boldsymbol{\sigma}_D(t), \boldsymbol{\varphi}_{\alpha k}(t), \boldsymbol{\phi}_{\alpha k,\alpha' k'}(t)\}$ [34,40]. A similar derivation of the TD-NFGF method can be found in Ref. [47], in which the Fermi-Dirac distribution is expended by using a partial fraction decomposition. The computational cost and memory requirements of the method could be reduced by transforming the auxiliary density matrices into vectors or scalars with the diagonalization of $\boldsymbol{\Lambda}_\alpha(\epsilon)$ [48]. In principle, the computational cost for the TD-NEGF method should depend on the number of atomic levels in the open system and the total number of the auxiliary density matrices $2N_k + 4N_k^2$ ($N_k = N_l + N_p$). The small values of N_l and N_p can obviously reduce the computational cost, but overly small values cannot preserve the accuracy of Lorentzian and Padé decomposition. In Sec. III A, we discuss the numerical validation of Lorentzian and Padé decomposition approach to obtain the appropriate values of N_l and N_p.

B. Electronic structures of edge-extended GNR systems

In this section, we examine the electronic structures of edge-extended GNR systems. As electron dynamics in the open system (the blue shaded part in Fig. 1) played a dominant role in our simulation, we first investigate the projected density of states (PDOS) for an open system, which was determined by both the Hamiltonian of the open system and the coupling to the environment. Within the NEGF method, the effect of coupling with the environment on the PDOS of open system is represented by the retarded self-energy $\boldsymbol{\Sigma}_\alpha^r(\epsilon)$,

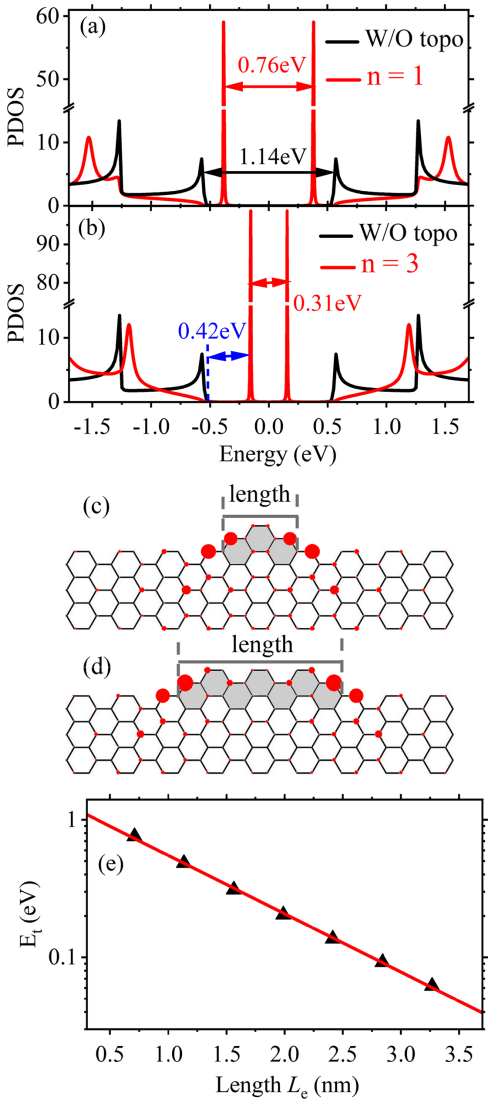

FIG. 2. The PDOS of open system (red line) for edge-extended GNR (a) $n = 1$ and (b) $n = 3$ comparing with the PDOS (black line) for pristine 7-AGNR without an edge-extended structure. The edge-extended structures would lead to in-gap topological states at energy of ± 0.38 eV (± 0.15 eV) for system $n = 1$ ($n = 3$). The density distribution of topological states for systems (c) $n = 1$ and (d) $n = 3$. The size of red circles denotes the amplitude of the density distribution. (e) The topological gap E_t varies with the length of edge-extended structure L_e for systems ($n = 1$–7).

and the PDOS can be given by [49]

$$N(\epsilon) = -\frac{1}{\pi}\mathrm{Im}\{\mathrm{Tr}[\epsilon \boldsymbol{I} - \boldsymbol{h}_D - \sum_{\alpha} \boldsymbol{\Sigma}_{\alpha}^{r}(\epsilon)]^{-1}\}, \tag{10}$$

where $\boldsymbol{h}_D$ is the Hamiltonian of an open system decoupled from the environment. The retarded self-energy includes a real part and an imaginary part: $\boldsymbol{\Sigma}_{\alpha}^{r}(\epsilon) = \boldsymbol{R}_{\alpha}(\epsilon) - i\boldsymbol{\Lambda}_{\alpha}(\epsilon)$. The imaginary part $\boldsymbol{\Lambda}_{\alpha}(\epsilon)$ is a spectral function and can be calculated using a highly convergent renormalization method [44,45]. The real part $\boldsymbol{R}_{\alpha}(\epsilon)$ can be computed by $\boldsymbol{\Lambda}_{\alpha}(\epsilon)$ via the Kramers-Kronig relation.

Figure 2(a) plots the PDOS of open system, where the black line denotes the simulation result for pristine 7-AGNR without an edge-extended structure, and the band gap is 1.14 eV. The red line denotes the result for 7-AGNR with the dimer $n = 1$, and it is clear that the edge-extended structure creates two topological states in the band gap of the 7-AGNR backbone. The in-gap states are the topologically derived highest-occupied molecular orbital (HOMO) and lowest-unoccupied molecular orbital (LUMO). We can see that the gap between the topological states is $E_t = 0.76$ eV, which indicates that the intracell coupling is $t_n = E_t/2 = 0.38$ eV, which is in excellent agreement with the previous simulation result from density function theory (DFT) [29].

For the system with dimer $n = 3$, the topological gap reduces to $E_t = 0.31$ eV, as shown in Fig. 2(b). Meanwhile, the gap between the valence (conduction) band and HOMO (LUMO) becomes 0.42 eV, which is larger than the topological gap E_t. The reduction of E_t relies on the fact that the intracell coupling t_n would be reduced with the increase in the length of the edge-extended structure L_e. As shown in Figs. 2(c) and 2(d), the length increases from $L_e = 0.71$ nm for $n = 1$ to $L_e = 1.56$ nm for $n = 3$ (the carbon–carbon bond length was set to 1.42 Å). The size of red circles in Figs. 2(c) and 2(d) donates the density distribution of the topological states (HOMO) for systems $n = 1$ and $n = 3$, respectively. The topological state of LUMO exhibits the same density distribution as the state of HOMO. Clearly, the topological states are mainly distributed on the two ends of the edge-extended structure. Thus, the increase in L_e would decouple the topological states on the two ends, leading to the reduction of intra-cell coupling t_n and topological gap E_t.

To further reveal the dependence of E_t on the length L_e, we calculate the PDOS for systems with ($n = 1$–7) to obtain the corresponding values of E_t, as shown by black points in Fig. 2(e). We can see an exponential decay of topological gap E_t as the length L_e, which can be fitted by the exponential function $E_t = 1.46\ \mathrm{eV} \times e^{-0.98L_e}$ [the red line in Fig. 2(e)]. In other words, the energy of topological states can be controlled by the structural construction for edge-extended GNR systems. The controllability of these in-gap states provides an efficient way to develop future photoelectric devices, as the energy gap of device dominates the process of photoexcitation and the generation of photocurrents. Here, we focus on the photocurrents induced by the few-cycle laser pulse and investigate the effect of in-gap states on the photocurrent.

III. RESULTS AND DISCUSSIONS

A. Numerical validation of the TD-NEGF method

We then investigate the electron dynamics driven by laser pulses for system $n = 1$, and the electron dynamics of open system is described by TD-NEGF method. The Lorentzian and Padé decomposition approaches are employed to reduce the computational cost of simulation. For the Lorentzian decomposition, the spectral function $\boldsymbol{\Lambda}_{\alpha}(\epsilon)$ is deconstructed into Lorentzian functions; see Eq. (8). $\boldsymbol{\Lambda}_{\alpha}(\epsilon)$ is an N-by-N matrix, and N denotes the number of atomic levels in the open system. Each element of the matrix $\boldsymbol{\Lambda}_{\alpha}(\epsilon)$ is a function varying with energy ϵ, and each element is fitted separately by a set of

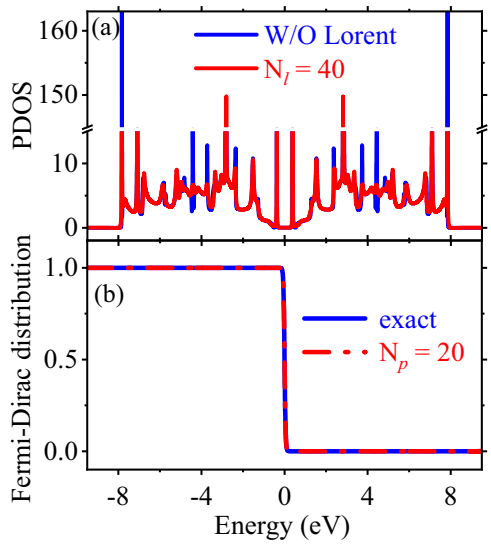

FIG. 3. (a) The simulation result of PDOS with Lorentzian decomposition ($N_l = 40$) compared with the result without the decomposition. (b) The Fermi-Dirac distribution deconstructed by Padé expansion ($N_p = 20$) comparing with the exact result.

Lorentzian functions. It is worth noting that the number of poles for Lorentzian functions N_l only depends on the centers Ω_l and widths W_l of Lorentzian functions, so all the elements of matrix $\mathbf{\Lambda}_\alpha(\epsilon)$ are fitted by a set of Lorentzian functions with fixed centers and widths $\{\Omega_l, W_l\}$, and each element of the coefficient matrix $\bar{\mathbf{\Lambda}}_{\alpha l}$ is determined separately via a least-squares fit. The strategy of finding optimal $\{\Omega_l, W_l\}$ is not unique, and may vary from system to system. In our simulation, the number of Lorentzian functions was set to $N_l = 40$. The centers Ω_l were located at 40 equally spaced energy points in the energy region $[-8.0\,\text{eV}, 8.0\,\text{eV}]$, and the widths W_l were set to the same value as the energy interval of these spaced points. For the Padé decomposition, the Fermi-Dirac distribution $f(\epsilon)$ is constructed via Eq. (9). The choice of N_p is related to the temperature of the system, as a lower temperature requires more Padé terms. In our simulation, the temperature is $T = 300$ K, and the number of Padé terms is set to $N_p = 20$.

The accuracy of Lorentzian and Padé decomposition is evaluated by the calculation of PDOS and the Fermi-Dirac distribution, respectively. The simulation results with and without the decomposition are compared in Figs. 3(a) and 3(b). As shown clearly, the results with the decomposition agree well with the results without the decomposition for both Lorentzian and Padé decomposition. This verifies that the Lorentzian and Padé decomposition is accurate in capturing the overall features of the electronic structure, especially for the equilibrium state. For nonequilibrium states, the accuracy of the decomposition is evaluated by the comparison of results of electron dynamics with a different number of N_l or with a different number of N_p.

We next consider the electron dynamics driven by a few-cycle laser pulse for system $n = 1$. The laser pulse is assumed to be linearly polarized light, and the direction of electric field is parallel to GNRs direction. To avoid the influence of DC component, we assume the electric field of a laser pulse to be an AC source and given by $E(t) = -\dot{A}(t)$ with the vector potential $A(t) = (E_0 t_c)/(2\pi)\exp[-t^2/(2t_d^2)]\sin(2\pi t/t_c + \varphi)$. Furthermore, the tunable parameters for the waveform of laser pulses include the carrier-envelope phase (CEP) φ, period time t_c, duration time t_d, and field amplitude E_0.

In the simulation, we assume that only the device region (open system) is under irradiation of the laser pulse, and the electrode regions (surrounding environment) are out of the range of laser irradiation. Experimentally, this nanometer-scale irradiation region may be realized with field enhancement around the narrow gaps between metal nanoparticles and sharp tips in colloidal gold particles [50]. The electric field of the laser pulse would lead to an on-site ramp in the device region. For the electrode regions, the electric field would result in a time-varying energy shift $\Delta_\alpha(t)$ for electrode α, including the shift of energy bands and the shift of Fermi energy $\mu_\alpha + \Delta_\alpha(t)$. The energy shift $\Delta_\alpha(t)$ is determined by the electric field of laser pulse $E(t)$ and the length of the device region L_D. The center of the device region is set to the zero point of the electric potential, so the energy shift $\Delta_\alpha(t)$ for electrodes are given by $\Delta_L(t) = -\Delta_R(t) = eE(t)L_D/2$. It is worth noting that the zero point of the electric potential can be set to an arbitrary position of the device, the change in zero position does not affect the calculation results. The parameters of the laser pulse are given by ($\varphi = 0$, $t_c = 20$ fs, $t_d = 0.6\,t_c$, $E_0 = 0.4$ V/nm), and the time-varying electric field is depicted in Fig. 4(a). The transient photocurrents flowing from the left electrode and flowing into the right electrode could be obtained by the dissipation term $I_L = -\text{Tr}[\boldsymbol{D}_L](I_R = Tr[\boldsymbol{D}_R])$, and the current passing through the device is calculated as the average current $I(t) = [I_L(t) + I_R(t)]/2$, which is shown in Fig. 4(b).

While this transient photocurrent on a femtosecond scale is usually too fast to be directly measured in the experiment, the corresponding transferred charge $Q_{tr}(t) = \int_{-\infty}^{t} dt'\ I(t')$ could be used to investigate the ultrafast electron dynamics. To validate the accuracy of Lorentzian and Padé decomposition, we compare the simulation results of $Q_{tr}(t)$ with different numbers of N_l and N_p in Figs. 4(d) and 4(e), respectively. In Fig. 4(d), we can see the result calculated with $N_l = 40$ is consistent with that of $N_l = 50$; and in Fig. 4(e), the result calculated with $N_p = 20$ is consistent with that of $N_p = 25$. This means that the Lorentzian decomposition with $N_l = 40$ and Padé decomposition with $N_p = 20$ are accurate in our simulation. Thus, we adopt $N_l = 40$ and $N_p = 20$ in the following calculations of this paper.

The accumulation charge inside the device region is calculated by $Q_{\text{acc}}(t) = \int_{-\infty}^{t} dt'\ [I_L(t') - I_R(t')]$, as shown in Fig. 5(a). We can see there is no accumulation charge in the device region, it relies on the fact that the value of the current flowing from the left electrode $I_L(t)$ is the same as the current flowing into the right electrode $I_R(t)$ due to the spatial symmetry of the system. Figure 5(b) plots the time evolution of induced electron density on atom 1 and atom 2 [as marked in Fig. 1(a)] inside the device $\Delta n_i(t) = n_i(t) - n_i^{\text{eq}}$, where $n_i(t) = \boldsymbol{\sigma}_{ii}(t)$ is the electron density of atom i at time t and n_i^{eq} is the electron density in the equilibrium state. The deviation of electron density from the equilibrium state indicates the charge redistribution inside the device region. The electric

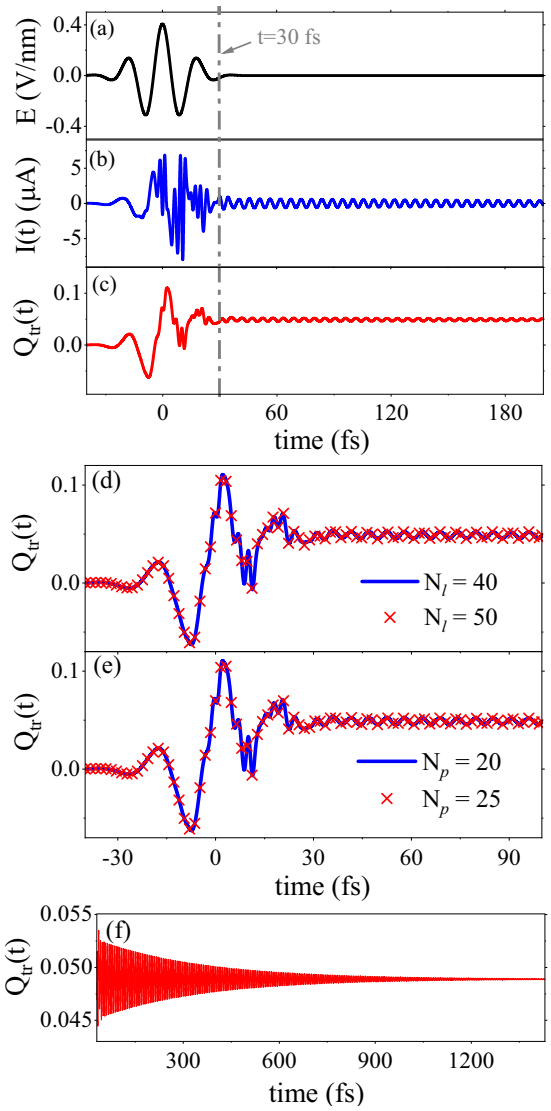

FIG. 4. (a) Time-varying electric field of the laser pulse with amplitude $E_0 = 0.4$V/nm and CEP $\varphi = 0$. (b) The corresponding photocurrent induced by the laser pulse. (c) The transferred charge $Q_{tr}(t)$ (time-integration of photocurrent) induced by the laser pulse. (d) The results of $Q_{tr}(t)$ computed with Lorentzian decomposition for $N_l = 40$ and $N_l = 50$. (e) The results of $Q_{tr}(t)$ computed with Padé decomposition for $N_p = 20$ and $N_p = 25$. (f) The time-varying transferred charge $Q_{tr}(t)$ after the laser pulse.

potential induced by this charge redistribution is not included in the tight-binding method used in our simulation, its effect on the photocurrents needs further investigations.

From Fig. 4(a), we can see the duration time t_d confines the laser pulse to the time region $[-30$ fs, 30 fs$]$. In this time region, the laser pulse drives the system out of the equilibrium state, and this region is the driven part of electron dynamics. For the time region $t > 30$ fs, the system gradually returns to the initial equilibrium state, and this region is the relaxation part of electron dynamics. Figures 4(c) and 4(f) show the simulation results of $Q_{tr}(t)$ during and after the pulse, respectively. It is clear that the transferred charge is mainly established at the driven part of electron dynamics. In the

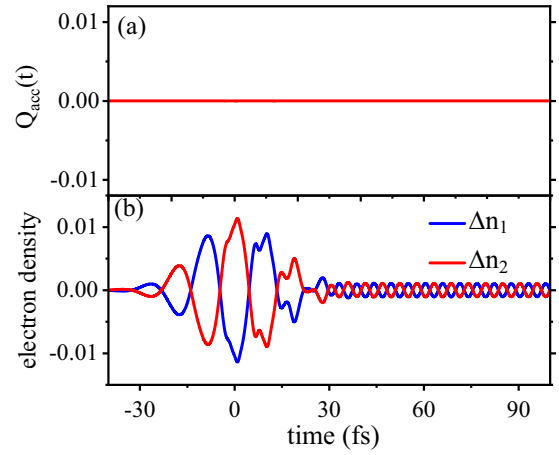

FIG. 5. (a) The accumulation charge inside the device region varying with the time. (b) The time evolution of induced electron density on atom 1 and atom 2 [as marked in Fig. 1(a)] inside the device.

relaxation part of electron dynamics ($t > 30$ fs), $Q_{tr}(t)$ is slightly oscillating around a fixed value. The frequency of the oscillation is found to be 0.76 eV, as determined by the topological gap of the system $n = 1$, as shown in Fig. 2(a). As time goes on, the nonequilibrium state of the system dissipates into the surrounding environment, and time-varying $Q_{tr}(t)$ tends toward a stable value [see Fig. 4(f)]. This stable value is defined as the total transferred charge $Q = Q_{tr}(\infty) = 0.049\,e$. Compared with the phototcurrent $I(t)$ varying on the femtosecond scale, the total transferred charge Q is much easier to measure in the experiment, so we focus on the dependence of Q on the waveform of the incident laser pulses in the following discussions.

B. Dependence of the transferred charge on the CEP and duration time of laser pulses

We then investigate the manipulation of the transferred charge by the CEP of laser pulses. The period time, duration time, and field amplitude of pulses were set to $t_c = 20$ fs, $t_d = 0.6\ t_c$, and $E_0 = 0.4$ V/nm, respectively. The CEP varies from 0 to 2π. For each point of CEP, we carry out the calculation of photocurrents for system $n = 1$ and obtain the stable transferred charge Q in a long-enough time. The simulation results, as shown by the red line in Fig. 6(a), exhibit a sinusoidal dependence of Q on the CEP φ. Q only includes a CEP-dependent component and varies around the value $Q = 0$ because of the spatial symmetry of the edge-extended 7-AGNR system, and this characteristic is also found in the simulation of the pristine 7-AGNR system [18]. However, this phenomenon is different from that in the simulation of laser-pulse-induced photocurrents in the dielectric system of α-SiO_2 [14] and tunneling barrier system [12] in which the transferred charges include a CEP-independent component owing to the spatial asymmetry of the system. For the systems in this paper, this CEP-independent component can be included by changing the Fermi level position of electrodes. For example, the Fermi level of the left electrode moves by 0.1 eV, and the Fermi level of the right electrode remains unchanged.

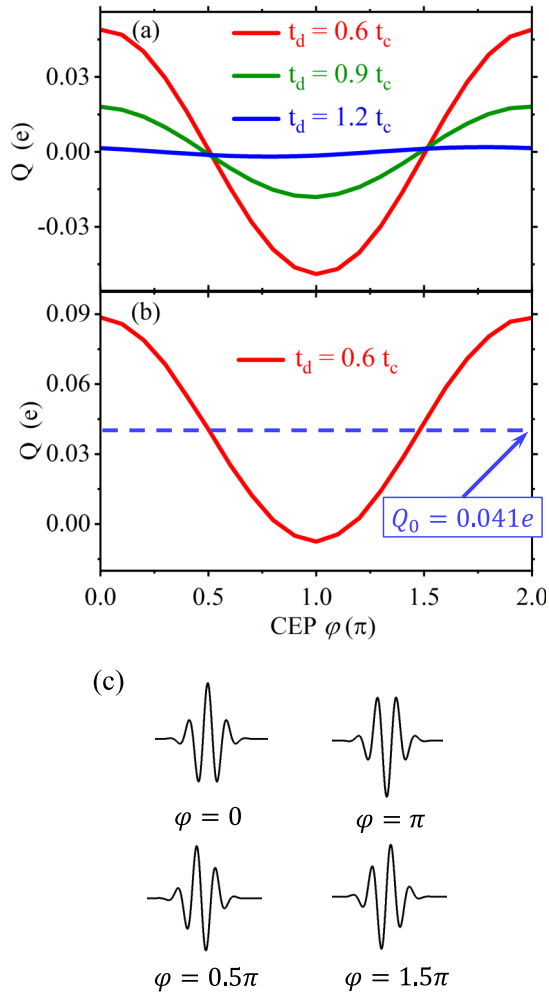

FIG. 6. (a) The transferred charge Q varying with the CEP of laser pulses ($t_c = 20$ fs and $E_0 = 0.4$ V/nm). The red line, green line, and blue line show the simulation results for duration time $t_d = 0.6\ t_c$, $0.9\ t_c$, and $1.2\ t_c$, respectively. (b) The transferred charge varying with CEP for the case of changing the Fermi level position of electrodes, the Fermi level of left electrode moves by 0.1 eV, and the Fermi level of right electrode remains unchanged. (c) The electric field of laser pulses for different CEPs with $t_d = 0.6\ t_c$.

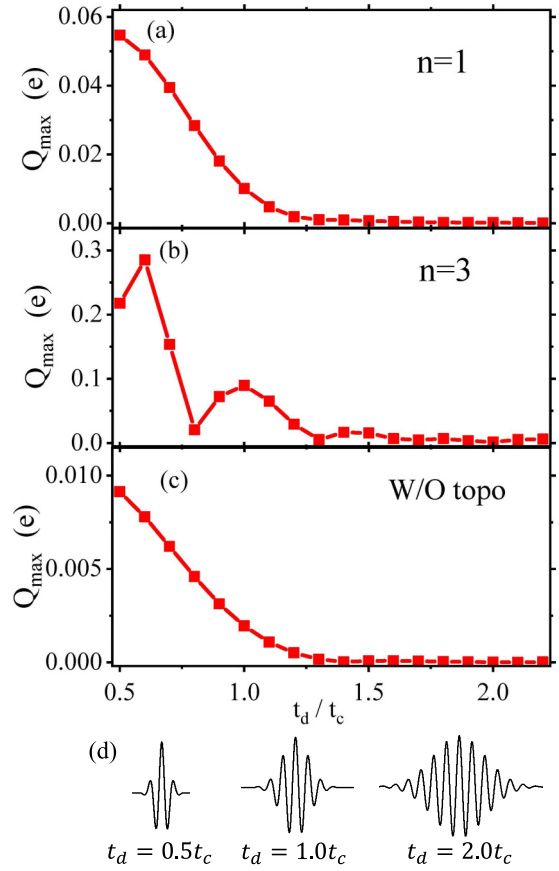

FIG. 7. The max values of the transferred charge Q_{max} varying with duration time t_d for systems (a) $n = 1$, (b) $n = 3$, and (c) without topological states. (d) The electric field of laser pules for different t_d with CEP $\varphi = 0$.

The corresponding results of the transferred charge are shown in Fig. 6(b). We can see the change in the Fermi level position can lead to a CEP-independent component of the transferred charge $Q_0 = 0.041\ e$.

The green line and blue line in Fig. 6(a) show the results for the duration time $t_d = 0.9\ t_c$ and $t_d = 1.2\ t_c$, respectively. We can see Q generally reduces with an increase in t_d, and this is more clear in the calculation of Q_{max} (the maximum value of Q for all CEP points) varying with t_d, as shown in Fig. 7(a). This result can be attributed to the fact that the transferred charge is generated from the asymmetry of a laser-pulse electric field. For example, take $t_d = 0.5\ t_c$ with $\varphi = 0$ [see Fig. 7(d)]. The maximum positive value of the electric field is significantly higher than the negative value, leading to an electron transfer from one side to another side of the GNR. With an increase in duration time, such as $t_d = 2.0\ t_c$, the difference in the positive and negative parts of the electric field becomes negligible, so the transferred charges tend toward zero.

In studies of the photoelectric conversion process under irradiation of stable incident light, an additional driving force, such as the built-in electric field around the *p*-*n* junction, is indispensable in generating a steady photocurrent. The built-in electric field usually involves chemical doping or a structural change of the semiconductor devices, resulting in the fabrication difficulty of photoelectric devices. In contrast, in this study, the electric-field asymmetry of a few-cycle laser pulse plays a similar role of a driving force without any change in devices. This provides a possible avenue for the further development of photoelectric devices.

To highlight the influence of topological states on the photoelectric response, we also calculate Q_{max} varying with t_d for the systems of edge-extended 7-AGNR ($n = 3$) and pristine 7-AGNR without topological states, as shown in Figs. 7(b) and 7(c), respectively. For all three systems, we find that the value of Q_{max} tends to zero when t_d is close to $1.5\ t_c$. Thus, in the study of laser-pulse-induced electron dynamics, the duration time of laser pulses should be short enough ($t_d < 1.5\ t_c$) to generate an obvious photoresponse. Moreover, the in-gap topological states lead to the enhancement of the transferred charge, and the values of Q_{max} for systems ($n = 1$ and $n = 3$) with topological states are much larger than the

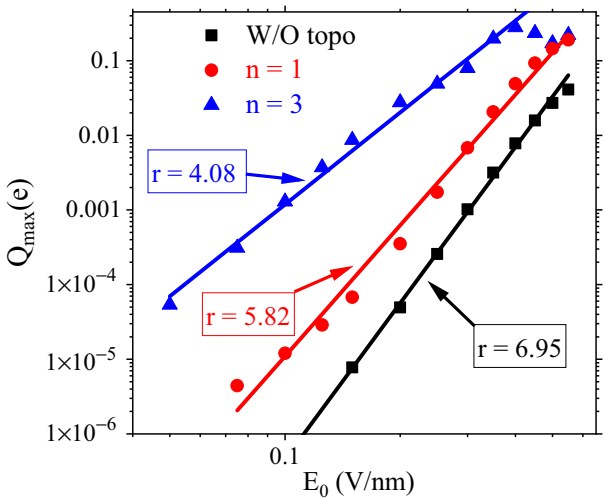

FIG. 8. The values of $Q_{\max}$ versus field amplitude E_0 of laser pulses on a log-log scale. The points of the simulation results can be fitted by a power-exponent function $Q_{\max} \propto E_0^r$. The power indexes are found to be $r = 6.95$, 5.82, and 4.08 for systems without topological states, $n = 1$, and $n = 3$, respectively.

values for system without topological states. For example, take $t_d = 0.6\ t_c$. The values of $Q_{\max}$ are 0.29 e, 0.049 e, and 0.0078 e for the systems $n = 3$, $n = 1$, and without topological states, respectively. In other words, the in-gap states of system $n = 3$ ($n = 1$) can enhance the transferred charge 37 (six) times compared with the system without topological states. This relies on the fact that the in-gap topological states can reduce the energy gap in the photoexcitation process and, consequently, enhance the intensity of the photoelectric response. This relation between topological states and the enhancement of photoelectric response becomes more clear with additional calculations of the transferred charge varying with the field amplitude of laser pulses, which is given in the next section.

C. Dependence of the transferred charge on the field amplitude of laser pulses

Then, we move on to examine the dependence of transferred charge on the field amplitude of laser pulses. The period time and duration time of laser pulses are set to $t_c = 20$ fs and $t_d = 0.6\ t_c$. Here, we consider the maximum value of transferred charge $Q_{\max}$ to avoid the influence of CEP φ. Figure 8 plots the values of $Q_{\max}$ versus field amplitude E_0 on a log-log scale, where the black points denote the results for system without topological states. These values of $Q_{\max}$ show a power-exponent relation to E_0 and can be fitted by the following function: $Q_{\max} \propto E_0^r$ (the black line in Fig. 8). The power index is found to be $r = 6.95$, which indicates that the three-photon absorption (3PA) and four-photon absorption (4PA) play a dominant role in the photoresponse. Similarly, for system $n = 1$ (red points in Fig. 8), the power index is found to be $r = 5.82$, which indicates that the 2PA and 3PA dominate the photoexcitation process. For system $n = 3$ (blue points in Fig. 8), the power index is $r = 4.08$, which

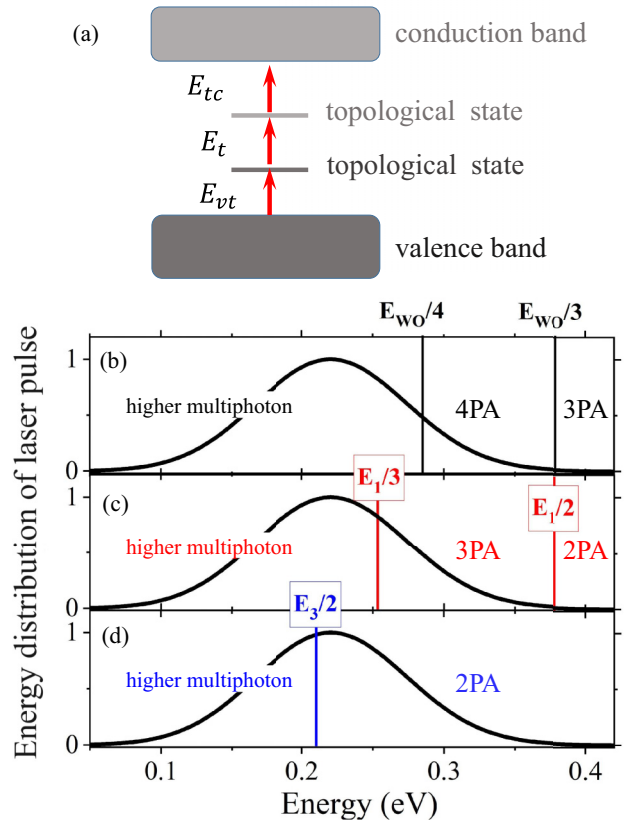

FIG. 9. (a) The photoexcitation process in systems with in-gap topological states. The relation between the energy distribution of laser pulses and the energy gaps for the system (b) without topological states, (c) $n = 1$, and (d) $n = 3$.

demonstrates that 2PA is the dominant photoexcitation process in the generation of photocurrent.

We can see that the order of multiphoton excitation is reduced for systems including in-gap topological states. This order reduction of multiphoton absorption increases the transition probability of photoexcitation and leads to the enhancement of the laser-pulse-induced photocurrent. The enhancement amplitude can increase by several hundreds of times, such as $E_0 = 0.2$ V/nm, and the value of $Q_{\max}$ (0.028 e) for a system $n = 3$ is 560 times larger than the value (5×10^{-5} e) for a system without topological states.

To understand the order reduction of multiphoton absorption, we further investigate the photoexcitation process in systems with in-gap topological states, as shown in Fig. 9(a). The photoexcitation process generally includes three steps: excitation from a valence band to a topological state, excitation between topological states, and excitation from a topological state to a conduction band. The corresponding energy gaps for these excitations are denoted as E_{vt}, E_t, and E_{tc}. From the simulation results of PDOS in Figs. 2(a) and 2(b), we can see that the energy gaps for system $n = 1$ are given by $E_{vt} = E_{tc} = 0.19$ eV, and $E_t = 0.76$ eV, and that the energy gaps for system $n = 3$ are given by $E_{vt} = E_{tc} = 0.42$ eV and $E_t = 0.31$ eV.

In the multiphoton excitation process, the transition probability is limited by the larger energy gap. For simplicity, we

only consider the largest energy gap among three excitation steps, which is $E_1 = 0.76\,\text{eV}$ ($E_3 = 0.42\,\text{eV}$) for system $n = 1$ ($n = 3$). Meanwhile, the energy gap for pristine 7-AGNR is the band gap of system $E_{\text{wo}} = 1.14\,\text{eV}$. The energy distribution of the laser pulses can be given by the Fourier transform of the time-varying electric field and can stay the same for different CEPs of the pulses.

The relation between the energy distribution of laser pulses and the energy gaps for the system without topological states, $n = 1$ and $n = 3$ are shown in Figs. 9(b), 9(c), and 9(d), respectively. For the system without topological states [see Fig. 9(b)], there is a significant distribution in the energy region ($E_{\text{wo}}/4 < E < E_{\text{wo}}/3$) and a small distribution in the region ($E_{\text{wo}}/3 < E < E_{\text{wo}}/2$), which leads to the dominant role of 4PA and 3PA in the multiphoton excitation process. For system $n = 1$ [see Fig. 9(c)], there is a significant distribution in the region ($E_1/3 < E < E_1/2$) and a small distribution in the region ($E_1/2 < E < E_1$), which results in the dominant role of 3PA and 2PA. Similarly, for system $n = 3$ [see Fig. 9(d)], the main distribution of laser pulse energy in the region ($E_3/2 < E < E_3$) leads to the dominant role of 2PA. It can be seen that the in-gap topological states can reduce the energy gap in the photoexcitation process. The smaller energy gap results in an order reduction of multiphoton absorption and enhances the photoresponse in the generation of the transferred charge.

IV. CONCLUSION

In summary, we investigated the laser-pulse-induced electron dynamics in 7-AGNR with and without topological states using the TD-NEGF method. The electric-field asymmetry of a few-cycle laser pulse drives the electron motion along the GNRs. The corresponding transferred charge Q can be controlled by the CEP of laser pulses. The CEP dependence of Q disappears with an increase in the duration time of laser pulses. Thus, in future investigations of laser-pulse-induced photocurrents, the duration time of laser pulses should be short enough ($t_d < 1.5\ t_c$) to generate an obvious photoresponse.

In contrast with the simulation results of pristine 7-AGNR system, the in-gap topological states in an edge-extended 7-AGNR system can be employed to enhance the laser-pulse-induced transferred charge. The enhancement amplitude of Q can reach several hundreds of times for the edge-extended 7-AGNR system $n = 3$. This enhancement is due to the reduction of the energy gap in the photoexcitation process, which reduces the order of multiphoton excitation and enhances the laser-pulse-induced photocurrent. In addition, the enhancement amplitude is related to the topological gap E_t of the edge-extended 7-AGNR system, and E_t can be adjusted by the length of the edge-extended structure. This provides a possible way to develop the carbon-based photoelectric device driven by few-cycle laser pulses.

ACKNOWLEDGMENTS

Support from the National Natural Science Foundation of China (Grant No. 21803035) and the Natural Science Foundation of Shandong province (Grant No. ZR2019BA013) is gratefully acknowledged.

[1] F. Krausz and M. Ivanov, Attosecond physics, Rev. Mod. Phys. **81**, 163 (2009).
[2] P. Dombi, Z. Pápa, J. Vogelsang, S. V. Yalunin, M. Sivis, G. Herink, S. Schäfer, P. Groß, C. Ropers, and C. Lienau, Strong-field nano-optics, Rev. Mod. Phys. **92**, 025003 (2020).
[3] F. Calegari, D. Ayuso, A. Trabattoni, L. Belshaw, S. De Camillis, S. Anumula, F. Frassetto, L. Poletto, A. Palacios, P. Decleva *et al.*, Ultrafast electron dynamics in phenylalanine initiated by attosecond pulses, Science **346**, 336 (2014).
[4] P. M. Kraus, B. Mignolet, D. Baykusheva, A. Rupenyan, L. Horný, E. F. Penka, G. Grassi, O. I. Tolstikhin, J. Schneider, F. Jensen *et al.*, Measurement and laser control of attosecond charge migration in ionized iodoacetylene, Science **350**, 790 (2015).
[5] C. M. Liu, J. Manz, K. Ohmori, C. Sommer, N. Takei, J. C. Tremblay, and Y. Zhang, Attosecond control of restoration of electronic structure symmetry, Phys. Rev. Lett. **121**, 173201 (2018).
[6] D. Hui, H. Alqattan, S. Yamada, V. Pervak, K. Yabana, and M. T. Hassan, Attosecond electron motion control in dielectric, Nat. Photon. **16**, 33 (2022).
[7] M. Garg and K. Kern, Attosecond coherent manipulation of electrons in tunneling microscopy, Science **367**, 411 (2020).
[8] T. Rybka, M. Ludwig, M. F. Schmalz, V. Knittel, D. Brida, and A. Leitenstorfer, Sub-cycle optical phase control of nanotunnelling in the single-electron regime, Nat. Photon. **10**, 667 (2016).
[9] K. Yoshioka, I. Katayama, Y. Minami, M. Kitajima, S. Yoshida, H. Shigekawa, and J. Takeda, Real-space coherent manipulation of electrons in a single tunnel junction by single-cycle terahertz electric fields, Nat. Photon. **10**, 762 (2016).
[10] M. Ludwig, G. Aguirregabiria, F. Ritzkowsky, T. Rybka, D. C. Marinica, J. Aizpurua, A. G. Borisov, A. Leitenstorfer, and D. Brida, Sub-femtosecond electron transport in a nanoscale gap, Nat. Phys. **16**, 341 (2020).
[11] Z. Hu, Y. Kwok, G. Chen, and S. Mukamel, Carrier-envelope-phase modulated currents in scanning tunneling microscopy, Nano Lett. **21**, 6569 (2021).
[12] R. Wang, F. Bi, W. Lu, X. Zheng, and C. Yam, Tracking electron dynamics of single molecules in scanning tunneling microscopy junctions with laser pulses, J. Phys. Chem. Lett. **12**, 6398 (2021).
[13] A. Schiffrin, T. Paasch-Colberg, N. Karpowicz, V. Apalkov, D. Gerster, S. Mühlbrandt, M. Korbman, J. Reichert, M. Schultze, S. Holzner *et al.*, Optical-field-induced current in dielectrics, Nature (London) **493**, 70 (2013).
[14] L. Chen, Y. Zhang, G. Chen, and I. Franco, Stark control of electrons along nanojunctions, Nat. Commun. **9**, 2070 (2018).
[15] S. Sederberg, D. Zimin, S. Keiber, F. Siegrist, M. S. Wismer, V. S. Yakovlev, I. Floss, C. Lemell, J. Burgdörfer, M. Schultze

et al., Attosecond optoelectronic field measurement in solids, Nat. Commun. **11**, 430 (2020).

[16] F. Langer, Y.-P. Liu, Z. Ren, V. Flodgren, C. Guo, J. Vogelsang, S. Mikaelsson, I. Sytcevich, J. Ahrens, A. L'Huillier *et al.*, Few-cycle lightwave-driven currents in a semiconductor at high repetition rate, Optica **7**, 276 (2020).

[17] S. Sederberg, F. Kong, F. Hufnagel, C. Zhang, E. Karimi, and P. B. Corkum, Vectorized optoelectronic control and metrology in a semiconductor, Nat. Photon. **14**, 680 (2020).

[18] R. Wang, F. Bi, W. Lu, X. Zheng, and C. Y. Yam, Theoretical investigation of electron dynamics driven by laser pulses in graphene nanoribbons, Phys. Rev. B **106**, 125305 (2022).

[19] L. Yang, C.-H. Park, Y.-W. Son, M. L. Cohen, and S. G. Louie, Quasiparticle energies and band gaps in graphene nanoribbons, Phys. Rev. Lett. **99**, 186801 (2007).

[20] H. Raza and E. C. Kan, Armchair graphene nanoribbons: Electronic structure and electric-field modulation, Phys. Rev. B **77**, 245434 (2008).

[21] A. Kimouche, M. M. Ervasti, R. Drost, S. Halonen, A. Harju, P. M. Joensuu, J. Sainio, and P. Liljeroth, Ultra-narrow metallic armchair graphene nanoribbons, Nat. Commun. **6**, 10177 (2015).

[22] R. Wang, F. Bi, W. Lu, and C. Yam, Tunable photoresponse by gate modulation in bilayer graphene nanoribbon devices, J. Phys. Chem. Lett. **10**, 7719 (2019).

[23] Y.-L. Lee, F. Zhao, T. Cao, J. Ihm, and S. G. Louie, Topological phases in cove-edged and chevron graphene nanoribbons: Geometric structures, $\mathbb{z}_2$ invariants, and junction states, Nano Lett. **18**, 7247 (2018).

[24] K.-S. Lin and M.-Y. Chou, Topological properties of gapped graphene nanoribbons with spatial symmetries, Nano Lett. **18**, 7254 (2018).

[25] Z. Chen, A. Narita, and K. Müllen, Graphene nanoribbons: On-surface synthesis and integration into electronic devices, Adv. Mater. **32**, 2001893 (2020).

[26] J. Li, S. Sanz, N. Merino-Díez, M. Vilas-Varela, A. Garcia-Lekue, M. Corso, D. G. de Oteyza, T. Frederiksen, D. Peña, and J. I. Pascual, Topological phase transition in chiral graphene nanoribbons: from edge bands to end states, Nat. Commun. **12**, 5538 (2021).

[27] R. K. Houtsma, J. de la Rie, and M. Stöhr, Atomically precise graphene nanoribbons: interplay of structural and electronic properties, Chem. Soc. Rev. **50**, 6541 (2021).

[28] D. J. Rizzo, G. Veber, T. Cao, C. Bronner, T. Chen, F. Zhao, H. Rodriguez, S. G. Louie, M. F. Crommie, and F. R. Fischer, Topological band engineering of graphene nanoribbons, Nature (London) **560**, 204 (2018).

[29] O. Gröning, S. Wang, X. Yao, C. A. Pignedoli, G. Borin Barin, C. Daniels, A. Cupo, V. Meunier, X. Feng, A. Narita *et al.*, Engineering of robust topological quantum phases in graphene nanoribbons, Nature (London) **560**, 209 (2018).

[30] Q. Sun, Y. Yan, X. Yao, K. Müllen, A. Narita, R. Fasel, and P. Ruffieux, Evolution of the topological energy band in graphene nanoribbons, J. Phys. Chem. Lett. **12**, 8679 (2021).

[31] X. Zheng, F. Wang, C. Y. Yam, Y. Mo, and G. H. Chen, Time-dependent density-functional theory for open systems, Phys. Rev. B **75**, 195127 (2007).

[32] C. Y. Yam, X. Zheng, G. H. Chen, Y. Wang, T. Frauenheim, and T. A. Niehaus, Time-dependent versus static quantum transport simulations beyond linear response, Phys. Rev. B **83**, 245448 (2011).

[33] S. Chen, Y. Kwok, and G. Chen, Time-dependent density functional theory for open systems and its applications, Acc. Chem. Res. **51**, 385 (2018).

[34] X. Zheng, G. Chen, Y. Mo, S. Koo, H. Tian, C. Yam, and Y. Yan, Time-dependent density functional theory for quantum transport, J. Chem. Phys. **133**, 114101 (2010).

[35] Y. H. Kwok, H. Xie, C. Y. Yam, X. Zheng, and G. H. Chen, Time-dependent density functional theory quantum transport simulation in non-orthogonal basis, J. Chem. Phys. **139**, 224111 (2013).

[36] H. Xie, F. Jiang, H. Tian, X. Zheng, Y. Kwok, S. Chen, C. Yam, Y. Yan, and G. Chen, Time-dependent quantum transport: An efficient method based on liouville-von-neumann equation for single-electron density matrix, J. Chem. Phys. **137**, 044113 (2012).

[37] R. Wang, X. Zheng, Y. Kwok, H. Xie, G. Chen, and C. Yam, Time-dependent density functional theory for open systems with a positivity-preserving decomposition scheme for environment spectral functions, J. Chem. Phys. **142**, 144112 (2015).

[38] Y. Zhang, S. Chen, and G. H. Chen, First-principles time-dependent quantum transport theory, Phys. Rev. B **87**, 085110 (2013).

[39] F. Covito, F. Eich, R. Tuovinen, M. Sentef, and A. Rubio, Transient charge and energy flow in the wide-band limit, J. Chem. Theory Comput. **14**, 2495 (2018).

[40] R. Wang, D. Hou, and X. Zheng, Time-dependent density-functional theory for real-time electronic dynamics on material surfaces, Phys. Rev. B **88**, 205126 (2013).

[41] R. Wang, W. Lu, H. Xie, X. Zheng, and C. Yam, Theoretical investigation of real-time charge dynamics in open systems coupled to bulk materials, J. Chem. Phys. **150**, 174119 (2019).

[42] Y.-W. Son, M. L. Cohen, and S. G. Louie, Energy gaps in graphene nanoribbons, Phys. Rev. Lett. **97**, 216803 (2006).

[43] A. H. Castro Neto, F. Guinea, N. M. R. Peres, K. S. Novoselov, and A. K. Geim, The electronic properties of graphene, Rev. Mod. Phys. **81**, 109 (2009).

[44] M. L. Sancho, J. L. Sancho, J. L. Sancho, and J. Rubio, Highly convergent schemes for the calculation of bulk and surface green functions, J. Phys. F: Met. Phys. **15**, 851 (1985).

[45] S.-H. Ke, H. U. Baranger, and W. Yang, Electron transport through molecules: Self-consistent and non-self-consistent approaches, Phys. Rev. B **70**, 085410 (2004).

[46] J. Hu, R.-X. Xu, and Y. Yan, Communication: Padé spectrum decomposition of fermi function and bose function, J. Chem. Phys. **133**, 101106 (2010).

[47] A. Croy and U. Saalmann, Propagation scheme for nonequilibrium dynamics of electron transport in nanoscale devices, Phys. Rev. B **80**, 245311 (2009).

[48] B. S. Popescu and A. Croy, Efficient auxiliary-mode approach for time-dependent nanoelectronics, New J. Phys. **18**, 093044 (2016).

[49] J. C. Cuevas and E. Scheer, *Molecular Electronics: An Introduction to Theory and Experiment* (World Scientific, Singapore, 2010).

[50] R. Alvarez-Puebla, L. M. Liz-Marzán, and F. J. García de Abajo, Light concentration at the nanometer scale, J. Phys. Chem. Lett. **1**, 2428 (2010).